Title

Compromise between band structure and phonon scattering in efficient n-Mg3Sb2-x Bi x thermoelectrics

Authors

Shi, Xuemin

Zhang, Xinyue

Ganose, Alexander

et al.

Publication Date

2021-05-01

DOI

10.1016/j.mtphys.2021.100362

Peer reviewed

Compromise between band structure and phonon scattering in efficient n-$Mg_3Sb_{2-x}Bi_x$ thermoelectrics

Xuemin Shi[1], Xinyue Zhang[1], Alexander Ganose[2], Junsoo Park[2], Cheng Sun[1], Zhiwei Chen[1], Siqi Lin[1], Wen Li[1], Anubhav Jain[2] and Yanzhong Pei[1,*]

[1]Interdisciplinary Materials Research Center, School of Materials Science and Engineering, Tongji Univ., 4800 Caoan Rd., Shanghai 201804, China.

[2]Lawrence Berkeley National Lab, 1 Cyclotron Rd, Berkeley, CA, USA

Correspondence: yanzhong@tongji.edu.cn

n-type Mg_3Sb_2-based materials have become a top candidate for efficient thermoelectric applications within 300-700K, due to its high band degeneracy, inherently high carrier mobility and low lattice thermal conductivity, as well as its advantages of less toxicity and abundance. Existing works showed that Mg_3Bi_2-alloying largely help ensure the exceptional performance, leaving a key issue to be uncovered on the primary mechanisms favoring or limiting the thermoelectric performance of $Mg_3Sb_{2-x}Bi_x$ alloys. Here we focus on the alloy composition dependent transport properties at various temperatures, with a large volume of experimental data. It is revealed that, with increasing x, the reduction in both inertial mass and lattice thermal conductivity is significantly beneficial, but the closure in band gap leads to a strong compensation due to the bipolar effect. Such a compromise between band structure and phonon scattering results in optimal Mg_3Bi_2-alloying concentrations to be about 50% ~ 75% at 300 K, 50% ~ 60% at 450K and 50% at 600 K, which successfully guiding this work to realize extraordinary thermoelectric figure of merit at these temperatures.

Introduction

Thermoelectricity is capable of a direct conversion between heat and electricity. This unique advantage together with its emission-free feature are distinguished virtues, while the low conversion efficiency of thermoelectric devices critically impedes its large-scale applications. Thermoelectric efficiency is largely determined by materials' dimensionless figure of merit, $zT = S^2\sigma T/\kappa$, where S, σ, κ and T are the Seebeck coefficient, electrical conductivity, thermal conductivity and absolute temperature, respectively. Note that thermal conductivity involves both lattice (κ_L) and electronic (κ_E) contributions.

Advanced thermoelectrics require materials possessing a high electrical conductivity and Seebeck coefficient, and a low thermal conductivity [2-4]. However, σ, S and κ_E are strongly coupled, which leads to the main strategies for improving zT being typified either by an enhancement in power factor (S^2/ρ) via band engineering[5-7], or by a suppression of κ_L through defect engineering[8-12]. In addition, the interaction between these physical parameters endows the importance of carrier concentration optimization in maximizing zT. All above strategies have brought about significant zT enhancements in many materials including GeTe[13-15], SnTe[16-18], PbTe[19-22], and Bi_2Te_3[23-26]. In recent years, n-type Mg_3Sb_2-based materials have been recognized as outstanding efficient thermoelectrics due to their high conduction band degeneracy[27, 28], intrinsically high carrier mobility[29-31] and low lattice thermal conductivity [32, 33], as well as the advantages of less toxicity and abundance.

Band structure, including the band degeneracy N_v, the inertial effective mass along the transport direction m_I^*, the intensity of charge scattering and the band gap E_g fundamentally determines the maximal thermoelectric performance once the material can be doped to have an optimal carrier concentration. The conduction band minimum of $Mg_3Sb_{2-x}Bi_x$ alloys locates along the L-M line with a valley degeneracy (N_v) of 6 while the valence band maximum locates around Γ point with a valley degeneracy of only 1[34-37]. This makes the thermoelectric performance of n-type much better than that of p-type. In addition to the large conduction band degeneracy, the electron inertial mass m_I^* of ~0.2 m_e for $Mg_3Sb_{2-x}Bi_x$ alloys was found to be sufficiently small to ensure a high mobility thus a high zT [38, 39].

With years of development, a few effective dopants are revealed to ensure a broad range of carrier concentration up to 10^{20} cm^{-3} for locating its optimum. These dopants are typified by group-III_B (Sc[40] and Y[41, 42]) and rare-earth (La[43, 44], Nd[45] and Pr[46]) cations for Mg and chalcogen (Te[27, 47], Se[48, 49]) anions for Sb. The low electron inertial mass m_I^* largely ensures an electron mobility to be as high as ~170 cm^2/V-s at 300 K, providing the grains are sufficiently large[50], grains are minimally oxidized[29], and the material is free of charge scattering sources other than acoustic phonons[29]. These scattering sources include ionized impurities[51, 52], secondary phases[53-56], and boundary potential barriers[35, 50, 57], which tend to exist in materials synthesized by a wet-chemical or a ball-milling approach. This further inspires a development in synthesis technique using a tantalum-sealing for melting and a nearly hot-deforming for sintering[29, 42] or similar ones including a post-annealing under a Mg-vapor [30, 58, 59].

Thermally, Mg_3Sb_2-based materials are found to be naturally strong in lattice anharmonicity[60], and small size of Mg cations[33] is believed to be favorable for soft vibrational modes. Both features lead the lattice thermal conductivity to be intrinsically low[32, 33, 61]. Furthermore, alloying reduces lattice thermal conductivity because of the strengthened phonon scattering by alloy defects[36, 62].

With all above efforts, Mg_3Sb_2-thermoelectrics, in particular, $Mg_3Sb_{2-x}Bi_x$ alloys have been realized to show a very bright future for efficient and eco-friendly applications within 300-700 K[31, 35, 42, 58]. However, the effect of band gap on the thermoelectric properties, has be much less focused on, of which the resultant strong bipolar conduction in these narrow gap materials might be critical[31, 35, 63]. This can be quite similar to the case of conventional Bi_2Te_3-thermoelectrics[4], of which the insufficient band gap size fundamentally limits its high efficiency to cover a temperature range of T>450 K.

In this study, a large number of existing results and additional experiments/calculations in $Mg_3Sb_{2-x}Bi_x$ alloys consistently show a smooth change with x in critical parameters determining the thermoelectric performance. This reveals the existence of a strong bipolar effect induced by the insufficient band gap, which offers a guidance for optimization and further improvements. This leads this work to locate the optimal alloy compositions for various working temperatures and to realize the corresponding extraordinary thermoelectric figure of merit zT of 0.8 at 300 K, 1.2 at 450 K and 1.6 at 600 K.

Results and Discussion

The details on synthesis, characterizations, measurements (Fig. S1) and calculations for $Mg_3Sb_{2-x}Bi_x$ are given in the supplementary. In order to ensure a high mobility, the materials are with coarse grains (tens of microns) enabled by a tantalum-sealing for melting and by a nearly hot-deforming for sintering[29]. This technique further enables an much less excess of Mg (~1.7%) than that in literature work (usually ~7%[47]) for ensuring a high doping efficiency, which might be helpful for less impurities as well. The corresponding powder X-ray diffraction (XRD) patterns are shown in Fig. S2. The observed diffraction peaks can be well indexed to those of Mg_3Sb_2 with a

$CaAl_2Si_2$ structural (space group of $P\bar{3}m1$[54, 64, 65]). Phase purity is further confirmed by scanning electron microscope (SEM) and energy dispersive spectrometer (EDS) analyses (Fig. S3). The lighter-color boundaries seen in the SEM images (Fig. S3) suggest a higher concentration of Bi, and the etching process promotes its formation. These Bi-rich boundaries have been frequently observed in the literatures[66, 67], and the reason can be an interesting topic deserving further investigations. Fortunately, the existence of Bi-rich boundaries shows no detrimental effects on mobility thus thermoelectric performance, as long as the grains are coarse enough[29, 42, 66]. The lattice parameters for $Mg_3Sb_{2-x}Bi_x$ alloys are shown in Fig. S4, showing an increase due to Mg_3Bi_2-alloying.

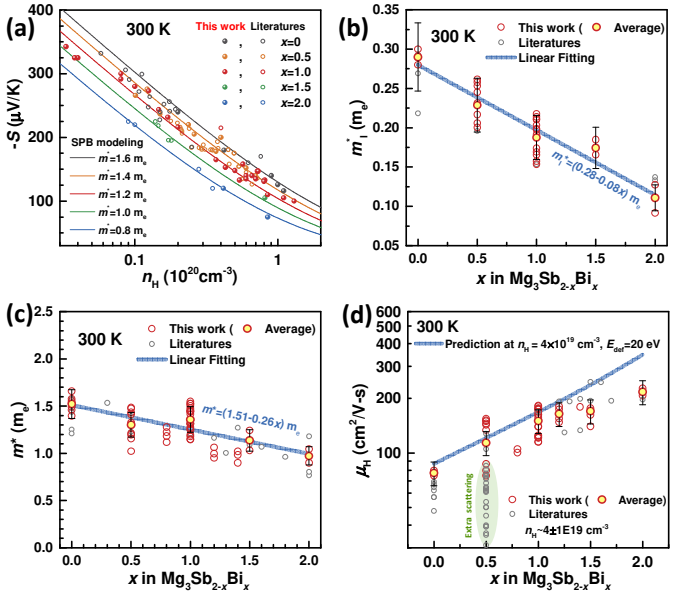

Fig. 1. Hall carrier concentration dependent Seebeck coefficient (a), composition dependent density-of-states mass m^* (b), inertial mass m^*_I (c) and Hall mobility μ_H (d) for n-type $Mg_3Sb_{2-x}Bi_x$ alloys at 300 K. Literature results[37, 43, 48, 51, 52, 62, 68, 69] are included for a comparison.

All the $Mg_3Sb_{2-x}Bi_x$ alloys in this work show a dominant charge scattering by acoustic phonons (Fig. S5). This enables a single parabolic band model (details in the supplementary) to approximate the charge transport properties (Fig. 1). With Mg_3Bi_2 alloying, the density-of-state effective mass (m^*) is found to decreases from 1.6 to 0.8 m_e. This can be largely understood by the decrease in the inertial effective mass (m^*_I, Fig. 1c and Fig. S6) determined by the optical measurements according to the Lyden method[70]. Therefore, the Hall mobility is found to increase at near-optimum carrier concentration (n_H) of ~4×10^{19} cm^{-3} with increasing Mg_3Bi_2-alloying, indicating that Mg_3Bi_2-alloying is indeed beneficial for enhancing the electronic performance since the maximal power factor (PF_{max}) is inversely proportional to inertial mass (m^*_I)[71]. Note that the much lower literature μ_H shown in Fig. 1d could be understood by the existence of charge scattering mechanisms other than acoustic scattering[37, 43, 48, 51, 52, 62, 68, 69].

According to the band structure calculations (Fig. 2), the conduction band minimum (CBM) locates roughly along the (L-M) direction. The exact coordinate for Mg_3Sb_2 is (0.42, 0, 0.33) in the Brillouin zone, which might show a small deviation depending on the computational techniques. Therefore, there are six symmetry-equivalent electron pockets for the CBM (a valley degeneracy of 6, $N_v = 6$). In case of Mg_3Bi_2, a negative gap of -0.15 eV (between Γ-K and L-M) is obtained in this work. These calculations are consistent with literature results[34] and the differences (minor if any) are due to the choice of pseudopotential, exchange-correlation functional, and the spin-orbit coupling effects[31, 72]. The detailed Fermi surfaces for a few electron densities are shown in Fig. S7 and Table. S1. Experimental Mg_3Bi_2-alloying dependent band gap in this work, according to the optical absorption measurements, reasonably agrees with the calculated ones and the literature results[72].

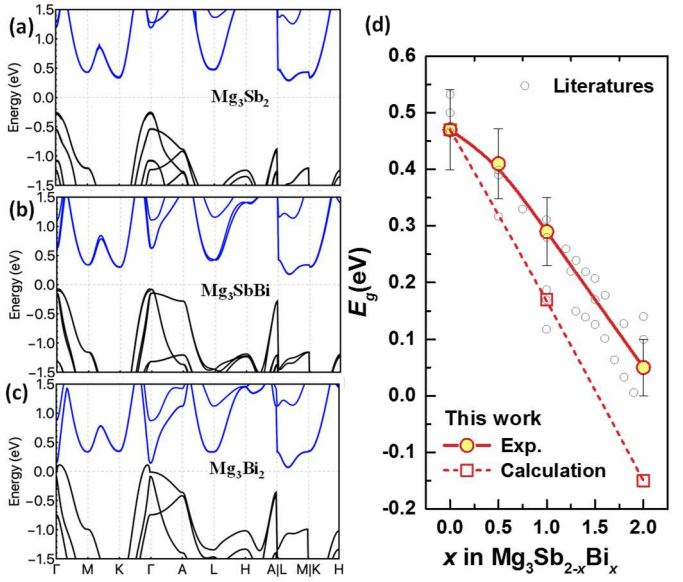

Fig. 2. Calculated band structures for Mg_3Sb_2 (a), Mg_3SbBi (b) and Mg_3Bi_2 (c), as well as the composition dependent band gap (d) for $Mg_3Sb_{2-x}Bi_x$ alloys, with a comparison to literature results[31, 3516].

As it is generally observed, ab initio calculations tend to underestimate the band gap particularly for Mg_3Bi_2 in this work. It is still not entirely clear weather Mg_3Bi_2 is a semimetal or a nearly zero-gap semiconductor. ab initio calculations usually show a negative bandgap of ~-0.1 eV[31, 34], so does this work. However, experimental results[31] on optical absorption and transport properties consistently suggest a degenerated semiconducting behavior in Mg_3Bi_2. As shown in Fig. 2d and S8, many literature measurements show a small but negative band gap of <0.15 eV in $Mg_3Sb_{2-x}Bi_x$ alloys at x>1.5. The argument of degenerately semiconducting behavior in Mg_3Bi_2 can further be supported by the large magnitude of $|S|$ (> 80 μV/K at T>300 K) and its continuous increase with increasing temperature[31]. Therefore, it should be reasonable to approximate Mg_3Bi_2 as a degenerate semiconductor even if it does have slightly overlapped conduction and valence bands. Note that the possible underestimation in band gap of Mg_3Bi_2 by ab initio calculations might further lead to an underestimation of the band gaps of $Mg_3Sb_{2-x}Bi_x$ alloys with high concentrations of Bi.

Weighted mobility enables a meaningful measure of electronic performance for thermoelectrics. Based on the single parabolic band model (SPB) with a charge scattering dominated by acoustic phonons, the deformation potential coefficient (E_{def}) and density-of-state effective mass (m^*) are estimated to be nearly independent with temperature and doping level (Fig. S9, and S10), largely simplifying the understanding on temperature dependent transport properties.

Taking linear fits to the alloy composition dependent m^*, m^*_I (Fig. 1b and 1c) and an average deformation coefficient E_{def} of 18 eV, the SPB model enables quantitative predictions on mobility at a certain electron concentration (Fig. 1d), maximal power factor (PF_{max}, Fig. 3a) and weighted mobility

(μ_w, Fig. 3b) for $Mg_3Sb_{2-x}Bi_x$ alloys at a few exemplary temperatures. With increasing x at x<1~1.5, the increase in μ_w and PF_{max} is primarily due to the reduction in m^*_I, which are further in good agreement with model predictions. The discrepancy between prediction and measurements at x>1~1.5 can therefore be attributed to the bipolar effect, since Mg_3Bi_2-alloying significantly reduces the band gap (<10 k_BT depending on temperature and composition). Furthermore, the bipolar effect gets stronger and the discrepancy gets larger at higher temperatures in heavily Mg_3Bi_2-alloyed compositions.

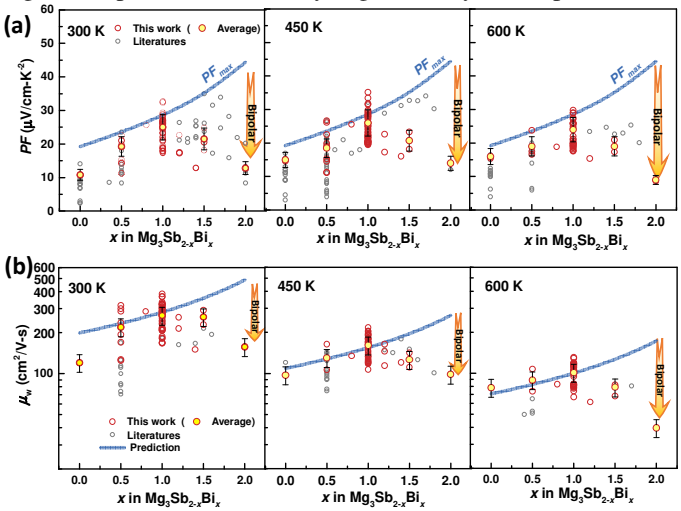

Fig. 3. Composition dependent power factor (a) and weighted mobility (μ_w, b) for n-type $Mg_3Sb_{2-x}Bi_x$ alloys at 300, 450 and 600 K, with a comparison to literature results[43, 48, 51, 52, 62, 68, 69] and model predictions.

With low phonon relaxation times due to a strong anharmonicity (i.e. a large Guneisen parameter of ~2, Table S2 and Fig. S10 and S11), pristine Mg_3Sb_2 shows a low lattice thermal conductivity. Room-temperature longitudinal (v_l), transverse (v_t) and mean (v_s) sound velocities decrease linearly with increasing x (Fig. 4a), which indicates a beneficial effect for reducing the lattice thermal conductivity (κ_L, more precisely κ-$L\sigma T$ with a Lorenz factor L determined by the SPB model) due to Mg_3Bi_2-alloying. Note that both calculated and measured κ_L (in the extrinsic conduction region) show a nearly 1/T dependence, indicating the dominance of phonon-phonon Umklapp scattering in these materials.

Taking into account the sound velocity change, the lattice thermal conductivity can be predicted for $Mg_3Sb_{2-x}Bi_x$ alloys, according to the Callaway model with the phonon dispersion considering the Born and von Karman periodic boundary conditions[12, 73-76] (details given in the supplementary with other estimated elastic parameters listed in Table S2). Due to the strong phonon scattering by large mass/strain fluctuations of Bi/Sb alloying defects and the strong reduction in sound velocity, the predicted κ_L decreases continuously with increasing Mg_3Bi_2-alloying (Fig. 4b-4d). Importantly and being quite similar to the case of x dependent electronic properties shown in Fig. 3, the bipolar effect gives a significant rise in κ-$L\sigma T$ at x>1~1.5 (particularly at high temperatures) as compared to that of model prediction.

In order to further ensure the reduction in v_s and the strengthening in phonon scattering due to Mg_3Bi_2-alloying, Raman spectrum with Lorentzian deconvolutions for $Mg_3Sb_{2-x}Bi_x$ alloys are shown in Fig. S12. The Raman peaks at about 2.1, 3.5 and 4.5 THz, respectively correspond to the TO_1, LO_1 and TO_2 modes of pristine Mg_3Sb_2. The shift of these peaks to lower frequencies consistently suggests the reduction in v_s due to Mg_3Bi_2-alloying (Fig. S12). Meanwhile, the broadening in the Full Width at Half Maximum (FWHM) at x~1 offers an important evidence of a broadening in phonon dispersion for a strong phonon scattering[20, 77].

The predicted composition dependent electronic and phononic properties (Fig. 1, 3 and 4), enable a full prediction in the maximum thermoelectric figure of merit zT_{max}. Indeed, Mg_3Bi_2-alloying enables both reductions in inertial mass and lattice thermal conductivity, which leads to a significant increase in predicted zT_{max} $Mg_3Sb_{2-x}Bi_x$ alloys (Fig. 5a-5c). However, the reduction in band gap due to Mg_3Bi_2-alloying simultaneously leads to a strong bipolar compensation in thermoelectric properties (detailed transport properties, reproducibility and stability are given in Fig. S10, S13 and S14). This leads experimentally realizable predicted zT_{max} to be limited in lightly Mg_3Bi_2-alloyed compositions and at low temperatures.

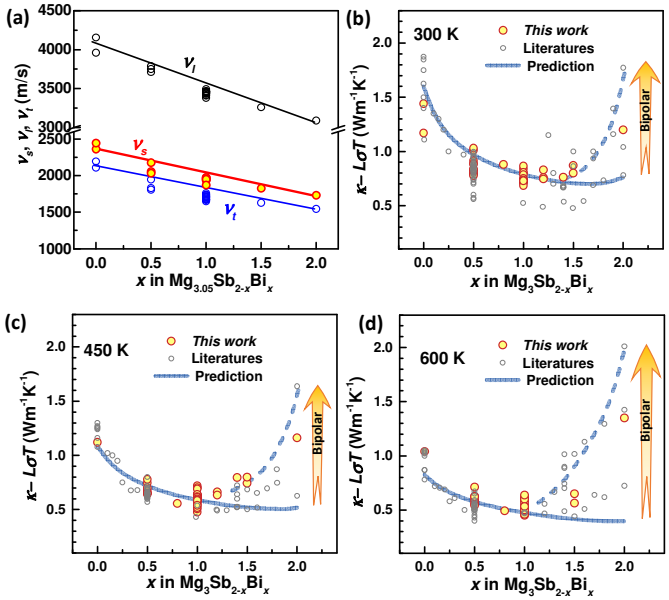

Fig. 4. Composition dependent sound velocity at 300 K (a) and lattice thermal conductivity (more precisely κ-$L\sigma T$) for n-$Mg_3Sb_{2-x}Bi_x$ alloys at 300 K (b), 450 K (c) and 600 K (d), with a comparison to literature results[29, 31, 33, 35, 37, 41-44, 51, 52, 57, 62, 66, 78, 79] and model predictions.

As the result of compromise between band structure and phonon scattering in n-$Mg_3Sb_{2-x}Bi_x$ alloys, this work respectively realizes extraordinary zTs of 0.8 @ 300 K, 1.2 @ 450 K and 1.6 @ 600 K in optimal Mg_3Bi_2-alloying contents of 50%~75%, 50%~60% and ~50% (Fig. 5d). Such a strong bipolar compensation is very similar to that of thermoelectric Bi_2Te_3[23-26], and n-$Mg_3Sb_{2-x}Bi_x$ alloys have shown very competitive performance for alternative applications. Moreover, n-$Mg_3Sb_{2-x}Bi_x$ alloys show top efficiency among all known n-type thermoelectrics[21, 24, 43, 57, 78-85] in a temperature range of 300-600 K.

Note there is a possibility of property-anisotropy due to the anisotropic crystal structure particularly in p-type conduction, according to directional solidification experiments[86] and theoretical calculations[60, 87]. Among the thermoelectric transport properties, resistivity is the most anisotropic and it differs by a factor of ~4.5 [87] between crystallographic directions along [001] and [101] in p-type Mg_3Sb_2. However in n-type conduction, the difference in resistivities along [001] and [101] is less than 20% [87]. Note that such an anisotropy is much weaker than that of conventional thermoelectric n-Bi_2Te_3, of which the resistivity can vary by a factor of >3 [88]. This rationalizes the observations in the

literatures[47, 60] a negligible property-anisotropy in polycrystalline n-type Mg_3Sb_2 thermoelectrics, including those with coarsen grains of >45 μm[42, 66]. In this work, a big chunk of $Mg_{3.085}Y_{0.015}SbBi$ with a Hall carrier concentration (~9×10^{19} cm^{-3}) slightly higher than its optimum is synthesized as well for property measurements along and perpendicular to the hot-press direction, which confirmed the effective property-isotropy as shown in Fig. S15.

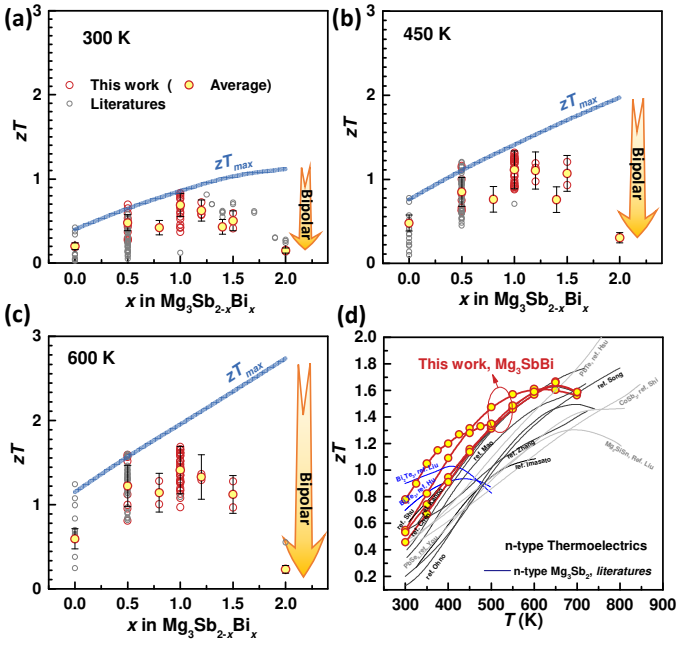

Fig. 5. Composition dependent thermoelectric figure of merit (zT) for n-type $Mg_3Sb_{2-x}Bi_x$ alloys at 300 K (b), 450 K (c) and 600 K (d), with a comparison to literature results[29, 31, 33, 35, 41-44, 48, 51, 52, 57, 62, 66, 68, 69, 78, 79] and model predictions; temperature dependent zT for $Mg_{3.05}SbBi$ obtained in this work, with a comparison to literature results for n-type thermoelectrics[21, 24, 37, 43, 57, 68, 78-85].

Furthermore, a single-leg device (2.5×2.5×6 mm^3) using the above mentioned big sample is fabricated for the efficiency measurement (Fig. S16). According to the literature results[31, 89-91] for a stable and conductive contact between the electrode and the thermoelectric material, both hot- and cold-side contacts are designed to include a 0.9 mm thick Ni electrode with a 0.1 mm thick Fe diffusion barrier layer in this work. Such a contact structure enables a contact resistance as low as 2.4 mΩ, corresponding to an interfacial contact resistance of ~11 μΩcm^2. This guarantees a measured maximum conversion efficiency as high as ~7% under a temperature gradient of ~400 K, which is very comparable to the predicted results based on the performance of thermoelectric material. Note the lower measured efficiency than the literature results[89-91] can be understood by the lower thermoelectric performance of the material used here for the single-leg device.

Summary

In summary, this work reveals the significantly beneficial effects of reductions in both electron inertial mass and phonon conductivity by Mg_3Bi_2-alloying for n-Mg_3Sb_2 thermoelectrics. Yet the simultaneous closure of band gap leads to a strong compensation due to the bipolar conduction of both electrons and holes. Such a compromise effectively guides this work to experimentally realize in optimal Mg_3Bi_2-alloying compositions extraordinary thermoelectric performances in these eco-friendly n-type Mg_3Sb_2-Mg_3Bi_2 alloys at different working temperatures. Importantly, this work indicates a further realization of the full thermoelectric extraordinariness of n-type Mg_3Sb_2-Mg_3Bi_2 alloys likely to be accomplished by a band gap engineering approach, for an even brighter future.

Acknowledgements

This work is supported by the National Natural Science Foundation of China (Grant No. 51861145305, 51772215 and 52001231), Fundamental Research Funds for Science and Technology Innovation Plan of Shanghai (18JC1414600) and "Shu Guang" Project Supported by Shanghai Municipal Education Commission and Shanghai Education Development Foundation. Computational work performed by AJ, JP, and AG was funded by the United States Department of Energy, Office of Basic Energy Sciences, Early Career Research Program. Lawrence Berkeley National Laboratory is funded by the DOE under award DE-AC02-05CH11231. This research used resources of the National Energy Research Scientific Computing Center (NERSC), a U.S. Department of Energy Office of Science User Facility operated under Contract No. DE-AC02-05CH11231.

Reference:

1. G. J. Snyder and E. S. Toberer, *Nat.Mater.*, 2008, **7**, 105-114.
2. Y. Pei, A. D. LaLonde, N. A. Heinz, X. Shi, S. Iwanaga, H. Wang, L. Chen and G. J. Snyder, *Adv. Mater.*, 2011, **23**, 5674-5678.
3. Z. Chen, X. Zhang and Y. Pei, *Adv. Mater.*, 2018, **30**, 1705617.
4. H. J. Goldsmid, *Introduction to Thermoelectricity*, Springer, Heidelberg, 2009.
5. Y. Pei, X. Shi, A. LaLonde, H. Wang, L. Chen and G. J. Snyder, *Nature*, 2011, **473**, 66-69.
6. F. J. DiSalvo, *Science*, 1999, **285**, 703-706.
7. S. Lin, W. Li, Z. Chen, J. Shen, B. Ge and Y. Pei, *Nat. Commu.*, 2017, **7**, 10287.
8. C. B. Vining, in *CRC handbook of thermoelectrics*, ed. D. M. Rowe, CRC Press, Boca Raton, Fla., 1995, ch. 28, pp. 329-337.
9. Z. Chen, Z. Jian, W. Li, Y. Chang, B. Ge, R. Hanus, J. Yang, Y. Chen, M. Huang, G. J. Snyder and Y. Pei, *Adv. Mater.*, 2017, **29**, 1606768.
10. S. I. Kim, K. H. Lee, H. A. Mun, H. S. Kim, S. W. Hwang, J. W. Roh, D. J. Yang, W. H. Shin, X. S. Li and Y. H. Lee, *Science*, 2015, **348**, 109-114.
11. Z. Chen, B. Ge, W. Li, S. Lin, J. Shen, Y. Chang, R. Hanus, G. J. Snyder and Y. Pei, *Nat Commun*, 2017, **8**, 13828.
12. Z. Chen, X. Zhang, S. Lin, L. Chen and Y. Pei, *National Science Review*, 2018, **5**, 888-894.
13. Z. Bu, W. Li, J. Li, X. Zhang, J. Mao, Y. Chen and Y. Pei, *Materials Today Physics*, 2019, **9**, 100096.
14. J. Li, X. Zhang, Z. Chen, S. Lin, W. Li, J. Shen, I. T. Witting, A. Faghaninia, Y. Chen, A. Jain, L. Chen, G. J. Snyder and Y. Pei, *Joule*, 2018, **2**, 976-987.
15. X. Zhang, Z. Bu, S. Lin, Z. Chen, W. Li and Y. Pei, *Joule*, 2020, **4**, 986-1003.
16. L. Zheng, W. Li, S. Lin, J. Li, Z. Chen and Y. Pei, *ACS Energy Letters*, 2017, **2**, 563-568.
17. W. Li, Y. X. Wu, S. Q. Lin, Z. W. Chen, J. Li, X. Y. Zhang, L. L. Zheng and Y. Z. Pei, *Acs Energy Letters*, 2017, **2**, 2349-2355.
18. J. Tang, B. Gao, S. Lin, J. Li, Z. Chen, F. Xiong, W. Li, Y. Chen and Y. Pei, *Adv. Funct. Mater.*, 2018, **28**, 1803586.
19. Y. Pei, Z. M. Gibbs, B. Balke, W. G. Zeier and G. J. Snyder, *Advanced Energy Materials*, 2014, **4**, 1400486.
20. Wu Yixuan, Chen Zhiwei , Nan Pengfei , Xiong Fen , Lin Siqi , Zhang Xinyue , Chen Yue , Chen Lidong , Ge Binghui and P. Yanzhong, *Joule*, 2019, **3**, 1276-1288.
21. K. F. Hsu, S. Loo, F. Guo, W. Chen, J. S. Dyck, C. Uher, T. Hogan, E. K. Polychroniadis and M. G. Kanatzidis, *Science*, 2004, **303**, 818-821.
22. Y. Xiao, Y. Wu, P. Nan, H. Dong, Z. Chen, Z. Chen, H. Gu, B. Ge, W. Li and Y. Pei, *Chem*, 2020, **6**, 523-537.
23. T. Chen, G. H. Guai, C. Gong, W. Hu, J. Zhu, H. Yang, Q. Yan and C. M. Li, *Energy & Environmental Science*, 2012, **5**, 6294-6298.
24. F. Li, R. Zhai, Y. Wu, Z. Xu, X. Zhao and T. Zhu, *Journal of Materiomics*, 2018, **4**, 208-214.

25. Q. Zhang, X. Ai, L. Wang, Y. Chang, W. Luo, W. Jiang and L. Chen, *Adv. Funct. Mater.*, 2015, **25**, 966-976.
26. C. Schumacher, K. G. Reinsberg, R. Rostek, L. Akinsinde, S. Baessler, S. Zastrow, G. Rampelberg, P. Woias, C. Detavernier, J. A. C. Broekaert, J. Bachmann and K. Nielsch, *Advanced Energy Materials*, 2013, **3**, 95-104.
27. J. Zhang, L. Song, S. H. Pedersen, H. Yin, L. T. Hung and B. B. Iversen, *Nat Commun*, 2017, **8**, 13901.
28. J. Shuai, J. Mao, S. Song, Q. Zhang, G. Chen and Z. Ren, *Materials Today Physics*, 2017, **1**, 74-95.
29. X. Shi, C. Sun, Z. Bu, X. Zhang, Y. Wu, S. Lin, W. Li, A. Faghaninia, A. Jain and Y. Pei, *Advanced science*, 2019, **6**, 1802286.
30. J. J. Kuo, Y. Yu, S. D. Kang, O. Cojocaru-Mirédin, M. Wuttig and G. J. Snyder, *Advanced Materials Interfaces*, 2019, **6**, 1900429.
31. Jun Mao, Hangtian Zhu, Zhiwei Ding, Zihang Liu, Geethal Amila Gamage, Gang Chen and Z. Ren, *Science*, 2019, **365**, 495-498.
32. M. B. Maccioni, R. Farris and V. Fiorentini, *Physical Review B*, 2018, **98**, 220301.
33. W. Peng, G. Petretto, G.-M. Rignanese, G. Hautier and A. Zevalkink, *Joule*, 2018, **2**, 1879-1893.
34. K. Imasato, S. D. Kang, S. Ohno and G. J. Snyder, *Materials Horizons*, 2018, **5**, 59-64.
35. K. Imasato, S. D. Kang and G. J. Snyder, *Energy & Environmental Science*, 2019, **12**, 965-971
36. X. Shi, X. Wang, W. Li and Y. Pei, *Small Methods*, 2018, **2**, 1800022.
37. Y. Pan, M. Yao, X. Hong, Y. Zhu, F. Fan, K. Imasato, Y. He, C. Hess, J. Fink, J. Yang, B. Büchner, C. Fu, G. J. Snyder and C. Felser, *Energy & Environmental Science*, 2020, **13**, 1717-1724
38. Y. Pei, A. D. LaLonde, H. Wang and G. J. Snyder, *Energy & Environmental Science*, 2012, **5**, 7963-7969.
39. Zhijia Han, Zhigang Gui, Y. B. Zhu, Peng Qin, Bo-Ping Zhang, Wenqing Zhang , Li Huang and W. Liu, *Research*, 2020, DOI: 10.34133/2020/1672051, DOI: 10.34133/32020/1672051.
40. P. Gorai, E. S. Toberer and V. Stevanović, *J. Appl. Phys.*, 2019, **125**, 025105.
41. S. W. Song, J. Mao, M. Bordelon, R. He, Y. M. Wang, J. Shuai, J. Y. Sun, X. B. Lei, Z. S. Ren, S. Chen, S. Wilson, K. Nielsch, Q. Y. Zhang and Z. F. Ren, *Materials Today Physics*, 2019, **8**, 25-33.
42. X. Shi, T. Zhao, X. Zhang, C. Sun, Z. Chen, S. Lin, W. Li, H. Gu and Y. Pei, *Adv. Mater.*, 2019, **31**, 1903387.
43. K. Imasato, M. Wood, J. J. Kuo and G. J. Snyder, *Journal of Materials Chemistry A*, 2018, **6**, 19941-19946.
44. Fan Zhang, Chen Chen, Shan Li, Li Yin, Bo Yu, Jiehe Sui, Feng Cao, Xingjun Liu, Zhifeng Ren and Q. Zhang, *Adv. Electron. Mater.* , 2020, **6**, 1901391.
45. J. Li, S. Zhang, F. Jia, S. Zheng, X. Shi, D. Jiang, S. Wang, G. Lu, L. Wu and Z.-G. Chen, *Materials Today Physics*, 2020, DOI: 10.1016/j.mtphys.2020.100269, 100269.
46. J. Li, F. Jia, S. Zhang, S. Zheng, B. Wang, L. Chen, G. Lu and L. Wu, *Journal of Materials Chemistry A*, 2019, **7**, 19316-19323.
47. H. Tamaki, H. K. Sato and T. Kanno, *Adv. Mater.*, 2016, **28**, 10182-10187.
48. J. Zhang, L. Song, A. Mamakhel, M. R. V. Jørgensen and B. B. Iversen, *Chem. Mater.*, 2017, **29**, 5371−5383.
49. Fan Zhang, Chen Chen, Honghao Yao, Fengxian Bai, Li Yin, Xiaofang Li, Shan Li, Wenhua Xue, Yumei Wang, Feng Cao, Xingjun Liu, Jiehe Sui and Q. Zhang, *Adv. Funct. Mater.*, 2019, **30**, 1906143.
50. J. J. Kuo, S. D. Kang, K. Imasato, H. Tamaki, S. Ohno, T. Kanno and G. J. Snyder, *Energy & Environmental Science*, 2018, **11**, 429-434.
51. J. Mao, J. Shuai, S. Song, Y. Wu, R. Dally, J. Zhou, Z. Liu, J. Sun, Q. Zhang, C. Dela Cruz, S. Wilson, Y. Pei, D. J. Singh, G. Chen, C. W. Chu and Z. Ren, *Proceedings of the National Academy of Sciences of the United States of America*, 2017, **114**, 10548-10553.
52. J. Shuai, J. Mao, S. Song, Q. Zhu, J. Sun, Y. Wang, R. He, J. Zhou, G. Chen, D. J. Singh and Z. Ren, *Energy & Environmental Science*, 2017, **10**, 799-807.
53. D. Ramirez, A. Gallagher, R. Baumbach and T. Siegrist, *J. Solid State Chem.*, 2015, **231**, 217-222.
54. L. M. Watson, C. A. W. Marshall and C. P. Cardoso, *J.Phys. F: Met. Phys.*, 1984, **14**, 113-121.
55. S. H. Kim, C. M. Kim, Y.-K. Hong, K. I. Sim, J. H. Kim, T. Onimaru, T. Takabatake and M.-H. Jung, *Materials Research Express*, 2015, **2**, 055903.
56. L. R. Jørgensen, J. Zhang, C. B. Zeuthen and B. B. Iversen, *Journal of Materials Chemistry A*, 2018, **6**, 17171-17176.
57. T. Kanno, H. Tamaki, H. K. Sato, S. D. Kang, S. Ohno, K. Imasato, J. J. Kuo, G. J. Snyder and Y. Miyazaki, *Appl. Phys. Lett.*, 2018, **112**, 033903.
58. M. Wood, J. J. Kuo, K. Imasato and G. J. Snyder, *Adv. Mater.*, 2019, **31**, e1902337.
59. Kazuki Imasato, Chenguang Fu, Yu Pan, Max Wood, Jimmy Jiahong Kuo, Claudia Felser and G. J. Snyder, *Adv. Mater.*, 2020, **23**, 1908218.
60. J. Zhang, L. Song, M. Sist, K. Tolborg and B. B. Iversen, *Nat. Commu.*, 2018, **9**, 4716
61. J. Xin, G. Li, G. Auffermann, H. Borrmann, W. Schnelle, J. Gooth, X. Zhao, T. Zhu, C. Felser and C. Fu, *Materials Today Physics*, 2018, **7**, 61-68.
62. J. Mao, Y. Wu, S. Song, Q. Zhu, J. Shuai, Z. Liu, Y. Pei and Z. Ren, *ACS Energy Letters*, 2017, 2245-2250.
63. Jeongjae Lee, Bartomeu Monserrat, Ieuan D. Seymour, Zigeng Liu, Siaˆn E. Dutton and C. P. Grey, *J Mater Chem A*, 2018, **6**, 16983.
64. C. L. Condron, S. M. Kauzlarich, F. Gascoin and G. J. Snyder, *J. Solid State Chem.*, 2006, **179**, 2252-2257.
65. J. Zhang, L. Song, G. K. Madsen, K. F. Fischer, W. Zhang, X. Shi and B. B. Iversen, *Nat Commun*, 2016, **7**, 10892.
66. X. Shi, C. Sun, X. Zhang, Z. Chen, S. Lin, W. Li and Y. Pei, *Chem. Mater.*, 2019, **31**, 8987-8994.
67. Y. Wang, X. Zhang, Y.-Q. Liu, J.-X. Zhang and M. Yue, *Chinese Physics B*, 2020, **29**, 067201.
68. X. Shi, C. Sun, Z. Bu, X. Zhang, Y. Wu, S. Lin, W. Li, A. Faghaninia, A. Jain and Y. Pei, *Advanced science*, 2019, 1802286.
69. J. Zhang, L. Song and B. B. Iversen, *Angew. Chem. Int. Ed.*, 2020, **59**, 4278-4282.
70. H. A. Lyden, *Physical Review*, 1964, **134**, A1106-A1112.
71. X. Zhang and Y. Pei, *npj Quantum Materials*, 2017, **2**, 68.
72. J. Zhang and B. B. Iversen, *J. Appl. Phys.*, 2019, **126**, 085104.
73. B. Abeles, *Phys. Rev. B: Condens. Matter Mater. Phys.*, 1963, **131**, 1906–1911.
74. J. Callaway and H. C. Vonbaeyer, *Phys. Rev.*, 1960, **120**, 1149–1154.
75. P. G. Klemens, *Phys. Rev.*, 1960, **119**, 507–509.
76. C. J., *Phys Rev* 1959, **113**, 1046–1051.
77. R. A. Cowley, *Rep. Prog. Phys.*, 1968, **31**, 123.
78. X. Chen, H. Wu, J. Cui, Y. Xiao, Y. Zhang, J. He, Y. Chen, J. Cao, W. Cai, S. J. Pennycook, Z. Liu, L.-D. Zhao and J. Sui, *Nano Energy*, 2018, **52**, 246-255.
79. R. Shu, Y. Zhou, Q. Wang, Z. Han, Y. Zhu, Y. Liu, Y. Chen, M. Gu, W. Xu, Y. Wang, W. Zhang, L. Huang and W. Liu, *Adv. Funct. Mater.*, 2018, **24**, 1807235.
80. L. Hu, H. Wu, T. Zhu, C. Fu, J. He, P. Ying and X. Zhao, *Advanced Energy Materials*, 2015, **5**, 1500411.
81. W.-S. Liu, Q. Zhang, Y. Lan, S. Chen, X. Yan, Q. Zhang, H. Wang, D. Wang, G. Chen and Z. Ren, *Advanced Energy Materials*, 2011, **1**, 577-587.
82. S. Ohno, K. Imasato, S. Anand, H. Tamaki, S. D. Kang, P. Gorai, H. K. Sato, E. S. Toberer, T. Kanno and G. J. Snyder, *Joule* 2018, **2**, 141-154.
83. X. Shi, S. Q. Bai, L. L. Xi, J. Yang, W. Q. Zhang, L. D. Chen and J. H. Yang, *J. Mater. Res.*, 2011, **26**, 1745-1754.
84. L. You, Y. Liu, X. Li, P. Nan, B. Ge, Y. Jiang, P. Luo, S. Pan, Y. Pei, W. Zhang, G. J. Snyder, J. Yang, J. Zhang and J. Luo, *Energy & Environmental Science*, 2018, **11**, 1848-1858.
85. X. Liu, T. Zhu, H. Wang, L. Hu, H. Xie, G. Jiang, G. J. Snyder and X. Zhao, *Advanced Energy Materials*, 2013, **3**, 1238-1244.
86. X. Li, H. Xie and B. Yang, *J. Appl. Phys.*, 2020, **127**, 195104.
87. F. Meng, S. Sun, J. Ma, C. Chronister, J. He and W. Li, *Materials Today Physics*, 2020, **13**, 100217.
88. H. Schemer and S. Scherrer, in *CRC handbook of thermoelectrics*, ed. D. M. Rowe, CRC Press, Boca Raton, FL, 1995, ch. 19.
89. L. Yin, C. Chen, F. Zhang, X. Li, F. Bai, Z. Zhang, X. Wang, J. Mao, F. Cao, X. Chen, J. Sui, X. Liu and Q. Zhang, *Acta Mater.*, 2020, **198**, 25-34.
90. C. Xu, Z. Liang, H. Shang, D. Wang, H. Wang, F. Ding, J. Mao and Z. Ren, *Materials Today Physics*, 2021, **17**, 100336.
91. Q. Zhu, S. Song, H. Zhu and Z. Ren, *J. Power Sources*, 2019, **414**, 393-400.

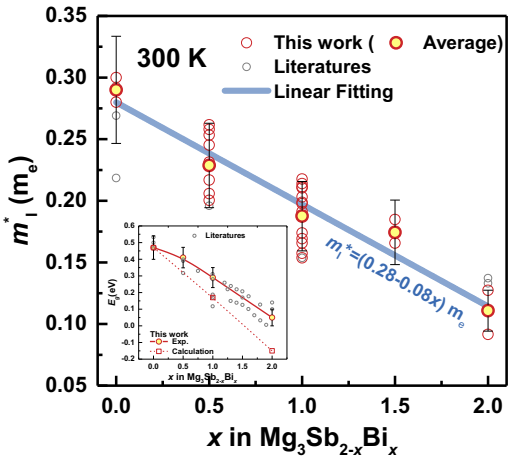
300 K
This work (Average)
Literatures
Linear Fitting
$m_l^*=(0.28-0.08x)\ m_e$
m_l^* (m_e)
x in $Mg_3Sb_{2-x}Bi_x$
E_g (eV)
Literatures
This work
Exp.
Calculation
x in $Mg_3Sb_{2-x}Bi_x$

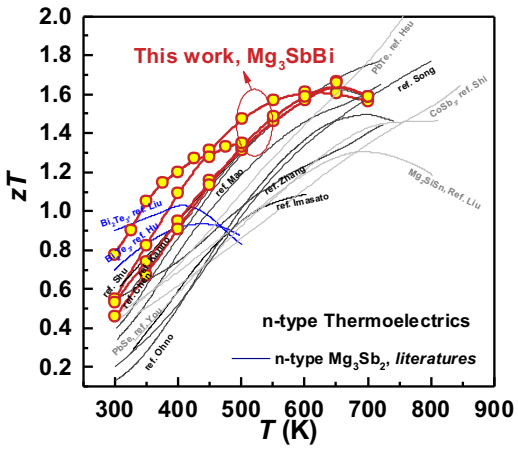
This work, Mg_3SbBi
n-type Thermoelectrics
n-type Mg_3Sb_2, *literatures*
zT
T (K)
ref. Song
ref. Shi
ref. Liu
ref. Imasato
ref. Ohno